

Acoustic charge transport induced by the surface acoustic wave in chemical doped graphene

Shijun Zheng, Hao Zhang, Zhihong Feng, Yuanyuan Yu, Rui Zhang, Chongling Sun, Jing Liu, Xuexin Duan, Wei Pang, and Daihua Zhang^{a)}

State Key Laboratory of Precision Measuring Technology and Instruments, Tianjin University, Tianjin 300072, China

(Received 4 September 2016; accepted 24 October 2016; published online 3 November 2016)

A graphene/LiNbO₃ hybrid device is used to investigate the acoustic induced charge transport in chemical doped graphene. The chemical doping of graphene via its physisorption of gas molecules affects the surface acoustic wave (SAW) charge carrier transport in a manner different from electric field drift. That transport induces doping dependent macroscopic acoustoelectric current. The chemical doping can manipulate majority carriers and induces unique acoustoelectric features. The observation is explained by a classical relaxation model. Eventually the device based on acoustoelectric current is proved to outperform the common chemiresistor for chemicals. Our finding provides insight into acoustic charge carrier transport during chemical doping. The doping affects interaction of carriers with SAW phonon and facilitates the understanding of nanoscale acoustoelectric effect. The exploration inspires potential acoustoelectric application for chemical detection involving emerging 2D nanomaterials. *Published by AIP Publishing.*
[\[http://dx.doi.org/10.1063/1.4967192\]](http://dx.doi.org/10.1063/1.4967192)

Surface acoustic waves (SAW) have proven to be a powerful technique to investigate the electronic properties of low dimensional systems, and tremendous progress have been achieved in the theoretical and experimental research regime ranging from exciton modulation, quantum conveyance, acousto-optical, and acousto-electric interplay.^{1–6} Among them, the interaction of SAW with electrons in two dimensional electron gases (2DEGs) has been fully exploited for the versatile, contactless manner of SAW.^{7–9} Such interaction includes acoustoelectric (AE) amplification and acoustoelectric attenuation. Both phenomena reflect the coupling of acoustic phonons (quantum of SAW) with charge carriers in semiconductor heterostructures. The acoustoelectric attenuation used in this paper, which induces acoustoelectric (AE) current, can help study the charge carriers transport mechanism in piezoelectric semiconductors under high magnetic fields and at low temperatures.^{10,11} In recent years, as low dimensional nanomaterials such as GaAs nanowire, graphene, and transition metal dichalcogenide (TMD) emerge, they have attracted significant attention from unique layered semiconductor devices realization because of their outstanding inherent physical properties in electronics and photonics. The atomically thin nanomaterials have a perfect crystal structure and flexible operability to construct 2D conductive channel compared with 2DEG heterostructures, so the integration of SAW and nanomaterials creates a promising experimental platform. It is made by attaching nanomaterials to various high quality crystal piezoelectric substrates such as lithium niobate (LiNbO₃) and aluminum nitride (AlN).^{12,13} The use of above high piezoelectric coupling coefficient substrates leads to a stronger moving electrostatic potential than that in 2DEG structures. Due to high carrier mobility of some nanomaterials, the integration enables

efficient charge carrier transport at room temperature to uncover distinct physical phenomenon.

Although that platform has inspired some innovative research of acoustoelectric effect referring to the popular 2D material-graphene, some physical acoustoelectric features remain unknown. The research on the dependence of AE current on majority carrier and concentration is of importance to further the understanding of charge carrier transport along the interface of 2D material and substrate.^{14–16} However, the information is little involved in the aforementioned work. It is supposed that the possible reason may be that the difficulty of solid gate fabrication on LiNbO₃ substrate and liquid gate causes significant acoustic loss inevitably.

In the work, the LiNbO₃ substrate is used to get strong moving electric field in MHz range. Because the monolayer graphene has excellent physisorption ability, chemical doping is adequately introduced to manipulate majority carriers and concentration. We focus on investigating the SAW charge carrier transport during graphene physisorption.^{17–19} The chemical doping enables a wide dynamic electrical modulation of graphene and avoids top-gate formation. Using this method, we observe chemical doping dependent ambipolar charge transport and unique AE current features. That result is explained by a classical relaxation model. In conclusion, the chemical doping can affect the interaction of acoustic phonon with charge carrier and thus change SAW charge carrier transport performance. Eventually we use the AE current to create a prototype of chemical detector that potentially outperforms the conventional type.

A schematic diagram of the device is shown in Fig. 1(a). A SAW delay line and two contacts in Fig. 1(a) are patterned on a 128°Y-cut LiNbO₃ substrate (10 × 10 mm). This orientation cut enables superior electro-mechanical coupling compared with the other cuts. The two contacts are defined on the acoustic path, with a separation of 10 μm. The interdigital

^{a)}dhzhang@tju.edu.cn

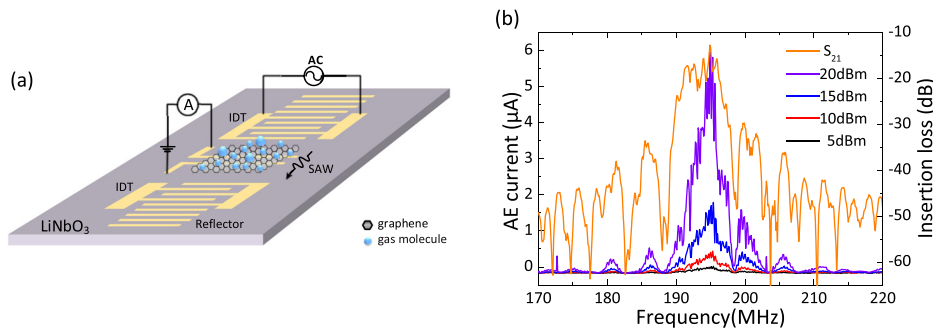


FIG. 1. (a) Schematic diagram of the hybrid graphene/LiNbO₃ device. The SAW induced by IDT propagates across the graphene on the acoustic path. (b) AE current-frequency traces at different RF power applied to IDT. Transmittance S_{21} forms between two IDTs. The AE current traces matches approximately with the profile of S_{21} under various input RF power.

transducer (IDT) consists of 25 pairs of electrodes alternately connected to two bus bars and 20 unconnected electrodes as SAW reflectors. The acoustic aperture of the IDT is 300 μm . The IDT generates SAW with a wavelength of $\lambda_{\text{SAW}} = 4\rho = 20 \mu\text{m}$, where ρ denotes the width of the IDT electrode ($\approx 5 \mu\text{m}$). The central frequency is $f = v_{\text{SAW}}/\lambda_{\text{SAW}} \approx 195.6 \text{ MHz}$.

Trivial Transfer Graphene[®] (TTG) (supplied by ACS Material) was used for device preparation. The TTG is picked up by LiNbO₃ chip in DI-water. The chip was rinsed in acetone to remove the PMMA on graphene, and then was spin coated with PMMA (80 K) as a barrier layer and photoresist (S1813). The graphene is patterned by photolithography and oxygen plasma etching (4 min; 40 mTorr; 70 W) (see [supplementary material](#), Fig. S1). Finally the residual photoresist with PMMA was stripped by acetone, and the chip was rinsed in IPA. The Van der Waals force enables close contact of the graphene with the LiNbO₃ substrate. The Raman spectroscopy used to confirm the graphene is monolayer (see [supplementary material](#), Fig. S2).

The chip is connected to a circuit board via the wire bond for measurements (see [supplementary material](#), Fig. S3). The transmittance S_{21} of the device is measured by a network analyzer (Agilent E5061B). The AE current is generated by applying a RF signal to IDT using a signal generator. A power amplifier is used to provide sufficient energy for the device. The AE current is 2-point measured by a semiconductor analyzer (Agilent B1500). The chemical doping is done in an aluminum chamber with N₂ diluted gas through two digital mass flow controllers.

The IDT induces a Rayleigh-type SAW that propagates along the X axis of LiNbO₃ substrate. SAW are propagating elastic vibrations confined to the surface of LiNbO₃ substrate.²⁰ The vibrations induced strain field creates a travelling piezoelectric potential field, which extends approximately one wavelength λ_{SAW} above the surface.²¹ When a graphene sheet is placed above the substrate within a distance of λ_{SAW} , the periodical potential can trap and convey packets of charge carriers in it at the SAW velocity.²² As a result, the interaction induces a measurable AE current.

The fluctuation of AE current closely following the IDTs transmittance S_{21} is shown in Fig. 1(b). The AE current magnitude is dependent on the RF power. Both AE current and the S_{21} reach a maximum at the central frequency of 195.6 MHz approximately. It means that the charge carriers can get the most portion of SAW power while the SAW attenuation reaches the maximum.² That power dependence

of AE current in the hybrid device is depicted by well-known Weinreich relations^{23–25}

$$j = \frac{\mu P_e f}{v_{\text{SAW}}^2} K_{\text{eff}}^2 \pi \left[\frac{\sigma_{2D}/\sigma_M}{1 + (\sigma_{2D}/\sigma_M)^2} \right]. \quad (1)$$

Here μ is the hole mobility of graphene, estimated to be 200–1000 cm²/V s. P_e is defined as the power of SAW, $P_e = P/Q_{\text{SAW}}$. $Q_{\text{SAW}} \approx 300$ is SAW device quality factor, and P is the total input power. v_{SAW} is the SAW velocity when the surface is shorted (about 3990 m/s in 128°Y-cut LiNbO₃), f is the SAW central frequency, K_{eff}^2 is the piezoelectric coupling coefficient (5.6% for LiNbO₃), and the current density has a maximum at a characteristic conductivity σ_M . For a hybrid system based on 128°Y-cut LiNbO₃, σ_M is approximately given by $\sigma_M = v_0 \epsilon_0 (\sqrt{\epsilon_{xx} \epsilon_{zz}} + 1) = 1.25 \times 10^{-6} \text{ S}$ where $\epsilon_0 = 8.85 \times 10^{-12} \text{ F/m}$ is the permittivity of free space and $\epsilon_{xx} \approx 85$ and $\epsilon_{zz} \approx 29.5$ are the dielectric constants of LiNbO₃ at constant stress. σ_{2D} is conductivity of graphene, $\sigma_{2D} \approx 9 \times 10^{-6} \text{ S}$. Inserting above values into Eq. (1) results in an AE current about 1.9–9.6 μA with 20 dBm total input power, which is in the same order of experimental value 5.9 μA in Fig. 1(b).

In this paragraph, the measurements of AE current at light chemical doping are carried out. The chemical doping is completed via venting 5 min NO₂ or NH₃ gas of defined concentration into a sealed chamber. Our device is mounted in that chamber and electrical connected with the semiconductor analyzer using microwave cables. A 2 mV bias and sweeping RF (180–210 MHz) are applied to the contacts and IDT, respectively. When out of IDT central frequency range, AE current is too small to be considered and direct current (DC) domains. Due to chemical doping, charge transfer between adsorbed gas molecules and carbon atoms leads to graphene conductance variation. It affects both AE and direct current electrically. The experimental results are presented in Figs. 2(a) and 2(b). Around the central frequency, the AE current variation is observed depending on the doping concentration. In the top part of Figs. 2(a) and 2(b), opposite to the well-known direct current response, the AE current declines when graphene suffers enhanced NO₂ p-doping. On the other side, the AE current rises when graphene suffers enhanced NH₃ n-doping. The normal change trends of direct current are shown in the bottom part of (a) and (b). Figs. 2(c) and 2(d) show the different relationship of AE and direct current with various doping concentrations. So far it is supposed that AE current is quite different from

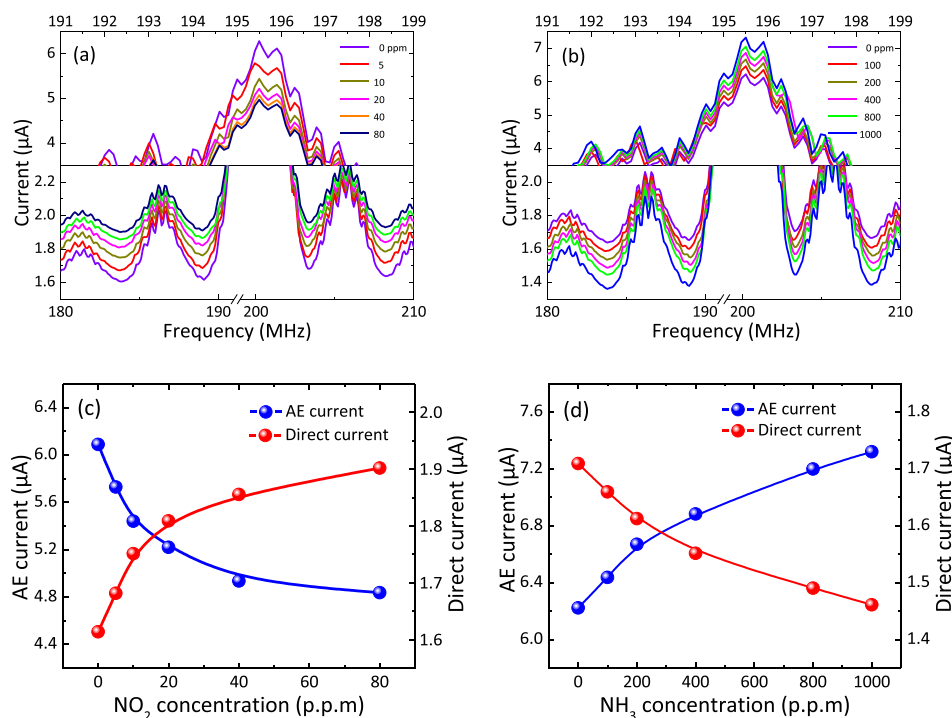


FIG. 2. Typical AE current-frequency traces at different gas molecular doping concentration: (a) p-doping using 5 min NO₂/N₂ gas mixture flow for each concentration; (b) n-doping using 5 min NH₃/N₂ gas mixture flow for each concentration. (c) and (d): AE/DC current variation comparison when graphene is exposed to NO₂/N₂ and NH₃/N₂ gas mixture flow of different concentrations, respectively.

electric field induced direct current. As predicted from Eq. (1), the AE current j has a non-monotonic dependence on a defined parameter β ($=\sigma_{2D}/\sigma_M$) theoretically. The AE current j is inversely proportional to β when $\beta > 1$; j is proportional to β when $\beta < 1$. In the extreme case of $\sigma_{2D} = \infty$, it is equivalent to metallized surface and the massive distributed carriers can screen the moving SAW accompanied potential field completely. Instead in the extreme case of $\sigma_{2D} = 0$, because it is to be analogous to an insulating surface, the potential field will be nearly the same as before due to the rather weak carriers screening effect. Both conditions above will not induce any AE current. If $\beta = 1$, the SAW power attenuation reaches the extreme, so maximum AE current appears theoretically.²⁰ Here if we assume that σ_{2D} is always higher than σ_M during light chemical doping, the AE current is inversely proportional to σ_{2D} with constant σ_M of LiNbO₃ substrate. When NO₂ keeps withdrawing electrons from graphene during physisorption of gas molecules, the enhanced p-doping of graphene increases σ_{2D} . Because free charge carriers can partially screen the SAW field as more and more holes are delocalized, the momentum transferred from SAW

to the carriers of graphene decreases, it explains the observation that AE current decreases as p-type doping concentration increases. The decreasing SAW attenuation leads to the AE current curve downshift. Replacing NO₂ as the hole dopant, NH₃ as an electron donor can provide electrons to recombine holes in slight p-type graphene. The σ_{2D} decreases in the presence of NH₃ doping, which coincides with the observation of the AE current increase. Figures 2(c) and 2(d) reveal the obvious opposite response of AE and direct current to NO₂ and NH₃ doping.

In the following paragraph, we investigate the influence of heavy chemical doping on AE current from the perspective of majority carriers transition in graphene. Based on the charge transfer mechanism that dominates in 2D nanomaterial chemiresistor, NH₃ is electron donor and NO₂ is electron acceptor. When the pristine graphene absorbs NO₂, it suffers p-doping because NO₂ withdraws electrons from it gradually.¹⁸ SAW transports holes and causes positive AE current shown in Fig. 3(a). When the pristine graphene absorbs NH₃ for enough long time, the majority carrier begins to transform from hole to electron. However, the SAW carrier

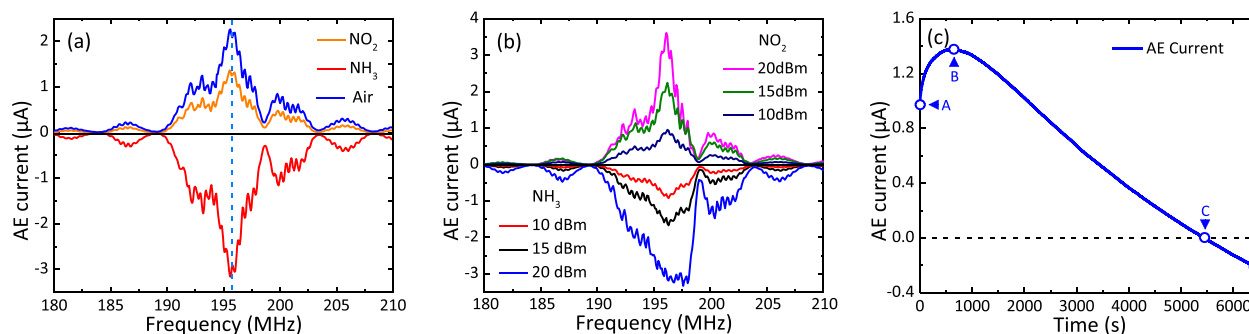


FIG. 3. (a) Different AE current-frequency traces when graphene is exposed to air, NO₂ and NH₃ for 5 min, respectively. (b) AE current-frequency traces at different types of heavy chemical doping in graphene. The AE currents of the opposite polarity are shown at different input RF power. (c) AE current-NH₃ flow time trace when a device works at SAW central frequency.

transport direction remains unchanged, so the direction of AE current will be reversed shown in Fig. 3(a). The ambient humidity influence is inevitable when the monolayer graphene is exposed to air.²⁶ Fig. 3(a) compares the AE currents in three different environments. The water could act as a p-dopant, leading to a shift of the Fermi-level in graphene.^{27,28} The p-doping increases the holes concentration, and decreases the AE current slightly due to carrier screening effect. To avoid the influence, the entire experiments were done in nitrogen, and the information obtained from measurements was collected in a sealed chamber. Moreover, the negative AE current also exhibits dependence on RF power as forward one shown is Fig. 3(b). It means that increased SAW power transferring from SAW to charge carriers induces increased AE current. Here we conclude that continuous chemical doping can change the majority carrier from hole to electron with the same SAW determined transport direction, so the AE current can be negative when the electrons are transported instead of holes. Contrary to AE current, the direct current is only dependent on the voltage bias regardless of majority carrier types. Such difference provides insight to judge the majority carrier types from AE current and the doping type is easily figured out. Figure 3(c) presents more results to demonstrate unique features of AE current in the condition of the heavy NH_3 doping. Different from the sweeping RF strategy adopted above, constant input RF manner is used here. The input RF keeps being at IDT central frequency and has a 10 dBm power. As 100 sccm 0.5% NH_3/N_2 mixture flow continues, the n-doping process makes graphene from light doped (point A) to heavy doped status, a threshold point B and zero point C of AE current appears in Fig. 3(c). Eventually the negative AE current turns up during a long time of NH_3 doping (point D). The downward parabolic profile (A-B-C) of AE current seems consistent with the model predication about the electrical transition from $\beta > 1$ to $\beta < 1$. The point B represents the $\beta = 1$ condition. The continuous NH_3 doping recombines the majority holes and enables $\beta < 1$ after a certain doping time. So the AE current starts to decrease (B to C). If the total holes are recombined by electrons from NH_3 charge transfer, zero AE current turns up at point C. After that, the electron becomes the majority carrier in graphene (C to D), so the AE current becomes negative. AE current changes at the threshold point C for majority carrier transition. The unique feature also appears on the other two different devices (see

supplementary material, Fig. S4). As mentioned above, chemical doping can change the AE current polarity but rather direct current, so only negative AE current can be observed during heavy doping. The demonstration reveals that the chemical doping of graphene via NH_3 molecules adsorption can influence the carriers screening effect and degrade SAW carrier transport performance. When the carrier concentration variation overwhelms the carriers screen effect, it makes AE current transform from being direct to inversely proportional to graphene conductance as heavy NH_3 doping happens.

In this paragraph, we demonstrate the potential chemical detection ability of the device based on the AE current. Some results are plotted in Fig. 4. The temporal opposite response of AE current and direct current (DC) for low NO_2 concentration is shown in Fig. 4(a). The limit of detection (LOD) seems to be 500 ppb in Fig. 4(b). Figure 4(c) demonstrates that the variation of AE current ($\Delta I/I$) outperforms direct current towards low NO_2 concentration. Furthermore, the detection performance of the AE current exhibits an average 150% improvement which is calculated from the conductance variation ratio in Fig. 4(c). Because the propagating SAW converts its electrostatic energy into the momentum of charge carrier, which is analogous to a kind of heating by the SAW moving potential field. Such heating process is distinctly unlike that produced by the drift electric field.⁹ Here the SAW transport strategy exhibits advantage over DC electric field drift in monolayer graphene. It possibly ascribes to a different charge carrier scattering effect between the two transport mechanisms. As a result, the AE current shows greater response towards chemicals than direct current during *in situ* measurement.

In conclusion, the demonstration of AE current response to chemical doping in monolayer graphene contributes to improve the physical insight of SAW carrier transport phenomena. The ambipolar charge carrier transport by SAW is realized via flexible chemical doping. The measured AE current polarity and magnitude exhibits dependence on the chemical doping concentration. In addition, we demonstrate unique electrical features of AE current for heavy NH_3 n-doping. The results are well consistent with the classical relaxation model description. Finally, the AE current exhibits an impressive electrical response to chemical doping. We confirm that chemical doping induced AE current variation can improve understanding the interaction of SAW with charge carriers.

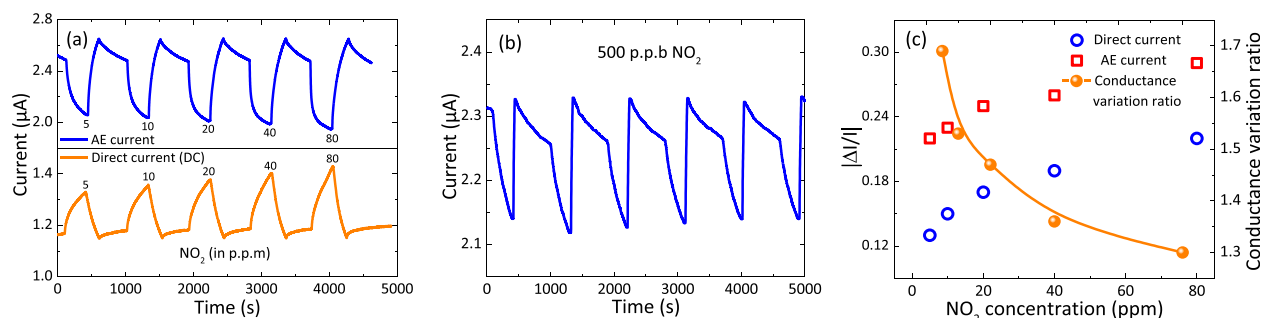


FIG. 4. (a) The AE current and direct current for low NO_2 doping concentration when AE/DC currents are generated by 15 dBm SAW power and 2 mV bias, respectively. (b) The limit of detection of AE current for NO_2 is 500 ppb. (c) Chemical doping induced AE/DC current variation ($\Delta I/I$) and chemical detection performance comparison.

We anticipate that the research could help realize versatile acoustoelectric chemical detector based on the emerging 2D nanomaterials.

See [supplementary material](#) for some details of the device and experimental data of three different devices.

The authors gratefully acknowledge the financial support by 111 Project (B07014) and Tianjin Applied Basic Research and Advanced Technology (13JKYBJC37100).

- ¹S. Tamura, "Acoustoelectric interaction of surface phonons in semiconductors. Effects of elastic anisotropy," *Phys. Rev. B* **20**, 1575 (1979).
- ²J. M. Shilton, D. R. Mace, V. I. Talyanskii, Yu. Galperin, M. Y. Simmons, M. Pepper, and D. A. Ritchie, "On the acoustoelectric current in a one-dimensional channel," *J. Phys. Condens. Matter* **8**, L337 (1996).
- ³J. B. Kinzel, D. Rudolph, M. Bichler, G. Abstreiter, J. J. Finley, G. Koblmüller, A. Wixforth, and H. Krenner, "Directional and dynamic modulation of the optical emission of an individual GaAs nanowire using surface acoustic waves," *Nano Lett.* **11**, 1512 (2011).
- ⁴A. Hernández-Mínguez, M. Möller, S. Breuer, C. Pfüller, C. Somaschin, S. Lazić, O. Brandt, A. García-Cristóbal, M. M. de Lima, Jr., A. Cantarero, L. Geelhaar, H. Riechert, and P. V. Santos, "Acoustically driven photon antibunching in nanowires," *Nano Lett.* **12**, 252 (2012).
- ⁵E. Preciado, F. J. R. Schülein, A. E. Nguyen, D. Barroso, M. Isarraraz, G. von Son, I.-H. Lu, W. Michailow, B. Möller, V. Klee, J. Mann, A. Wixforth, L. Bartels, and H. J. Krenner, "Scalable fabrication of a hybrid field-effect and acousto-electric device by direct growth of monolayer MoS₂/LiNbO₃," *Nat. Commun.* **6**, 8593 (2015).
- ⁶S. Hermelin, S. Takada, M. Yamamoto, S. Tarucha, A. D. Wieck, L. Saminadayar, C. Bäuerle, and T. Meunier, "Electrons surfing on a sound wave as a platform for quantum optics with flying electrons," *Nature* **477**, 435 (2011).
- ⁷C. Fischler, "Acoustoelectric amplification in a many-carrier system," *Appl. Phys. Lett.* **41**, 1439 (1970).
- ⁸M. Rotter, W. Ruile, G. Scholl, and A. Wixforth, "Novel concepts for GaAs/LiNbO₃ layered systems and their device applications," *IEEE Trans. Ultrason., Ferroelectr., Freq. Control* **47**, 242 (2000).
- ⁹Z. Insepov, E. Emelin, O. Kononenko, D. V. Roshchupkin, K. B. Tnyshchybayev, and K. A. Baigarin, "Surface acoustic wave amplification by direct current-voltage supplied to graphene film," *Appl. Phys. Lett.* **106**, 023505 (2015).
- ¹⁰A. Wixforth, J. Scriba, M. Wassermeier, J. P. Kotthaus, G. Weimann, and W. Schlapp, "Surface acoustic waves on GaAs/Al_xGa_{1-x} as heterostructures," *Phys. Rev. B* **40**, 7874 (1989).
- ¹¹I. L. Drichko, V. A. Malyshev, I. Yu. Smirnov, A. V. Suslov, O. A. Mironov, M. Kummer, and H. von Känel, "Acoustoelectric effects in very high-mobility p-SiGe/Ge/SiGe heterostructure at low temperatures in high magnetic fields," *J. Appl. Phys.* **114**, 074302 (2013).
- ¹²V. Miseikis, J. E. Cunningham, K. Saeed, R. O'Rourke, and A. G. Davies, "Acoustically induced current flow in graphene," *Appl. Phys. Lett.* **100**, 133105 (2012).
- ¹³Y. Chen, H. X. Zhang, H. Zhang, Z. H. Feng, H. Y. Zhao, C. L. Sun, S. J. Zheng, W. Pang, and D. H. Zhang, "Acoustically induced current in graphene by aluminum nitride transducers," *Appl. Phys. Lett.* **108**, 033107 (2016).
- ¹⁴L. Bandhu, L. M. Lawton, and G. R. Nash, "Macroscopic acoustoelectric charge transport in graphene," *Appl. Phys. Lett.* **103**, 133101 (2013).
- ¹⁵T. Poole, L. Bandhu, and G. R. Nash, "Acoustoelectric photoresponse in graphene," *Appl. Phys. Lett.* **106**, 133107 (2015).
- ¹⁶L. Bandhu and G. R. Nash, "Temperature dependence of the acoustoelectric current in graphene," *Appl. Phys. Lett.* **105**, 263106 (2014).
- ¹⁷F. Schedin, A. Geim, S. Morozov, E. Hill, P. Blake, M. Katsnelson, and K. Novoselov, "Detection of individual gas molecules adsorbed on graphene," *Nat. Mater.* **6**, 652 (2007).
- ¹⁸O. Leenaerts, B. Partoens, and F. M. Peeters, "Adsorption of H₂O, NH₃, CO, NO₂, and NO on graphene: A first-principles study," *Phys. Rev. B* **77**, 125416 (2008).
- ¹⁹R. Lv, G. Chen, Q. Li, A. McCreary, A. Botello-méndez, and S. V. Morozov, "Ultrasensitive gas detection of large-area boron-doped graphene," *Proc. Natl. Acad. Sci. U.S.A.* **112**, 1 (2015).
- ²⁰C. Rocke, S. Zimmermann, A. Wixforth, and J. P. Kotthaus, "Acoustically driven storage of light in a quantum well," *Phys. Rev. Lett.* **78**, 4099 (1997).
- ²¹M. M. D. Lima, Jr. and P. V. Santos, "Modulation of photonic structures by surface acoustic waves," *Rep. Prog. Phys.* **68**, 1639 (2005).
- ²²P. J. Leek, M. R. Buitelaar, V. I. Talyanskii, C. G. Smith, D. Anderson, G. A. C. Jones, J. Wei, and D. H. Cobden, "Charge pumping in carbon nanotubes," *Phys. Rev. Lett.* **95**, 256802 (2005).
- ²³G. Weinreich, "Acoustodynamic effects in semiconductors," *Phys. Rev.* **104**, 321 (1956).
- ²⁴M. Rotter, W. Ruile, D. Bernklau, H. Riechert, and A. Wixforth, "Giant acoustoelectric effect in GaAs/LiNbO₃ hybrid," *Appl. Phys. Lett.* **73**, 2128 (1998).
- ²⁵M. Rotter, A. Kalameitsev, A. O. Govorov, W. Ruile, and A. Wixforth, "Charge conveyance and nonlinear acoustoelectric phenomena for intense surface acoustic waves on a semiconductor quantum well," *Phys. Rev. Lett.* **82**, 2171 (1999).
- ²⁶K. Xu, P. Cao, and J. R. Heath, "Graphene visualizes the first water adlayers on mica at ambient conditions," *Science* **329**, 1188 (2010).
- ²⁷C. Melios, A. Centeno, A. Zurutuza, V. Panchal, C. E. Giusca, S. Spencer, S. Ravi, P. Silva, and O. Kazakova, "Effects of humidity on the electronic properties of graphene prepared by chemical vapor deposition," *Carbon* **103**, 273 (2016).
- ²⁸A. N. Sidorov, K. Gaskill, M. Buongiorno Nardelli, J. L. Tedesco, R. L. Myers-Ward *et al.*, "Charge transfer equilibria in ambient-exposed epitaxial graphene on (0001) 6H-SiC," *J. Appl. Phys.* **111**, 113706 (2012).